# Study of cycle-to-cycle dynamic characteristics of adiabatic Compressed Air Energy Storage using packed bed Thermal Energy Storage

He, Wei; Wang, Jihong; Wang, Yang; Ding, Yulong; Chen, Haisheng; Wu, Yuting; Garvey, Seamus

*DOI:*
10.1016/j.energy.2017.11.016



*Document Version*
Publisher's PDF, also known as Version of record

*Citation for published version (Harvard):*
He, W, Wang, J, Wang, Y, Ding, Y, Chen, H, Wu, Y & Garvey, S 2017, 'Study of cycle-to-cycle dynamic characteristics of adiabatic Compressed Air Energy Storage using packed bed Thermal Energy Storage', *Energy*, vol. 141, pp. 2120-2134. https://doi.org/10.1016/j.energy.2017.11.016

Energy 141 (2017) 2120–2134

Contents lists available at ScienceDirect

Energy

journal homepage: www.elsevier.com/locate/energy

# Study of cycle-to-cycle dynamic characteristics of adiabatic Compressed Air Energy Storage using packed bed Thermal Energy Storage

Wei He [a], Jihong Wang [a, b, *], Yang Wang [a], Yulong Ding [c], Haisheng Chen [d], Yuting Wu [e], Seamus Garvey [f]

[a] School of Engineering, University of Warwick, Coventry, CV4 7AL, United Kingdom
[b] School of Electrical & Electronic Engineering, Huazhong University of Science & Technology, China
[c] Birmingham Centre for Energy Storage, School of Chemical Engineering, University of Birmingham, Birmingham, B15 2TT, United Kingdom
[d] Institute of Engineering Thermophysics, Chinese Academy of Sciences, Beijing, 100190, China
[e] Key Laboratory of Enhanced Heat Transfer and Energy Conservation, Beijing University of Technology, Beijing, China
[f] Faculty of Mechanical Engineering, University of Nottingham, Nottingham, NG7 2RD, United Kingdom

ARTICLE INFO

*Article history:*
Received 9 April 2017
Received in revised form
11 October 2017
Accepted 5 November 2017
Available online 14 November 2017

*Keywords:*
Adiabatic compressed air energy storage
Packed bed thermal energy storage
Cycle-to-cycle modelling
Steady-state performance

ABSTRACT

The main challenge for analysing system time-dependent performance of Compressed Air Energy Storage (CAES) is the complexity of the system dynamic characteristics arisen from the thermal, mechanical, chemical and electrical sub-processes. Identification of time-variant interactions between these sub-processes is essential to understand, optimise and control transient behaviour of CAES systems in practice. Therefore, this study proposed a new detailed cycle-to-cycle modelling framework to dynamically simulate an adiabatic CAES (A-CAES) system with packed bed Thermal Energy Storage (PBTES). The detailed cycle-to-cycle modelling framework resolves the dynamics of associated components, links the time-variant performance of the components in each cycle, and simulates how the system performs from the start-up to the steady-state cycle operation. The framework provides a basis for further time-dependent analysis and control of both the components and the system. Using the model, two A-CAES systems using packed bed thermal stores, one filled with rock and the other one filled with encapsulated phase change material (PCM), were analysed and compared. The time-resolved simulation indicated a higher steady-state cycle efficiency of 56.5% for the system with the PCM-filled PBTES, versus 53.2% of the system with the rock-filled PBTES.



## 1. Introduction

Compressed Air Energy Storage (CAES) and Pumped Hydro Energy Storage are two major commercialised bulk energy storage technologies [1]. There are two CAES plants in operation and several CAES plants are being constructed or to be constructing worldwide [2,3]. The first utility-scale CAES project is the 290 MW (upgraded to 321 MW in 2006) Huntorf plant in Germany, which was built in 1978. The other is a 110 MW plant with a capacity of 26 h in McIntosh, Alabama. In recent years, adiabatic CAES (A-CAES) was proposed to avoid using fossil fuels. A-CAES combines Thermal Energy Storage (TES) to store compression heat during the system charging period, and reuses it instead of combustion to enhance air exergy before the stage of expansion during the discharge period.

Compared to conventional CAES plants, the performance of A-CAES systems significantly depends on the system cycle efficiency (also called round-trip efficiency) due to single energy input (which is electricity) of a typical A-CAES system. As a consequence, the performance of every component in the system becomes important. Any energy loss of components from charging to discharging influences the overall performance of an A-CAES system. Particularly, efficiencies of compressors and turbines were identified as two of the most sensitive factors [4]. Recently, experimental data of a low-temperature A-CAES using pressurised water as the thermal fluid was published by Wang et al. [5]. Average cycle efficiency of the pilot "TICC-500" plant was 22.6% [5]. The low efficiency was

* Corresponding author.School of Engineering, University of Warwick, Coventry, CV4 7AL, United Kingdom.
*E-mail address:* Jihong.wang@warwick.ac.uk (J. Wang).

https://doi.org/10.1016/j.energy.2017.11.016

mainly caused by the reduced components' efficiency from the design values [5], when they were operated at an operational window due to the interactions between components.

As indicated by these early-stage numerical and experimental data, detailed studies focusing on dynamic system performance and off-design operations of components are essential to analyse the time-dependent performance. A model which can resolve the time-dependent interactions between components and their performance variations significantly help optimally design the system operation. The dynamic model at both component- and system-level is a basis for further integration with controllers to ensure the identified optimal configuration operated in a operational window stably and robustly. However, there is lack of appropriate tools and methodologies from the literature to investigate the system dynamics by resolving the cycle-to-cycle performance of all the major components. Prior investigations primarily focused on the dynamic modelling of heat storage in A-CAES systems. Barbour et al. derived an A-CAES system model in which the sensible heat packed bed Thermal Energy Storage (PBTES) was dynamically simulated [6]. The results suggested that the main losses occur in compressors and expanders rather than in packed beds, indicating future detailed analysis of A-CAES systems with sophisticated compression and expansion modelling, and construncing and testing the A-CAES prototypes would be of value [6]. Wolf carried out a study of dynamic simulation of an A-CAES system using high-temperature TES, in which TES was modelled using finite element method, and compressor and turbine were modelled using empirical polynomial models [7]. Peng et al. presented a transient concentric-dispersion model of a PBTES filled with encapsulated phase change material (PCM) using the enthalpy method [8]. Their modelling showed the importance of the PBTES design (diameter and height of the vessel) to the overall system performance, and suggested a performance-improved A-CAES system by integrating with a heat recuperator [9,10]. However, most of these studies considered a constant efficiency for compressors/expanders in the system, and time-variant off-design performance of these machines was not considered. In addition, because most prior investigations used thermodynamic models or empirical models for simulating compressors/expanders, effects of design specifications or types of compressors/expanders were not considered at the system-level dynamic performance.

Although Sciacovelli et al. recently investigated how heat storage dynamics inducing the effect of off-design conditions to other components [11], the study used empirical models of compressors and expanders, and only sensible heat storage was considered. In fact, the latent heat of melting gives PCM significantly enhanced energy storage capacity. This high-capacity latent heat storage theoretically occurs isothermally and normally in a fairly narrow temperature range. These advantages let PCM-based heat storage promising and developing rapidly in the building-related applications [12] and the solar energy powered applications [13,14]. Different from these applications, a considerably wide range of storing temperature possibly exists in A-CAES, since a variable pressure ratio of compressors is caused by the isochoric air storage, e.g. storing air in salt caverns. Therefore, the performance of latent heat storage in A-CAES systems, and how the characteristic thermal dynamics affecting other components and the system are essential to design and operate an efficient A-CAES system with latent heat storage.

Therefore, the focus of this study was to develop a detailed modelling framework for analysing the A-CAES dynamics. The modelling framework is a method to simulate the A-CAES system transience. On one hand, the time-variant performance of both system and components are obtained by resolving the time-variant air dynamics from component to component in every cycle. On the other hand, the air flow is significantly affected by the design and control parameters at both system-level and component-level. Furthermore, a detailed cycle-to-cycle analysis of a selected system configuration was carried out using the proposed model. The analysis elucidated why the A-CAES system with the PCM-filled PBTES has higher steady-state cycle efficiency than that of the A-CAES system with the rock-filled PBTES.

## 2. System configuration

Fig. 1 illustrates the configuration of the studied A-CAES system, in which single-stage compression and single-stage expansion are used with a PBTES tank. In the charge period, air is first compressed by a reciprocating piston machine. After flowing through the PBTES, exergy of the compressed air is partially transferred and stored in the form of heat. The remaining exergy of the compressed air is stored in a storage tank. A heat exchanger is placed before the storage tank to control air temperature at the inlet of the storage tank. The studied A-CAES system employs a constant volume (isochoric) storage tank to store the air. Additionally, in the system discharging, the compressed air flows into the PBTES to increase its internal energy. A pressure regulator stabilises the operational unsteadiness and maintains a nearly constant inlet pressure to turbine.

At the early stage of the A-CAES detailed cycle-to-cycle dynamic modelling, a simple configuration with single-stage compression and single-stage expansion is selected in this study. Although the modelled simple system configuration may be not economically feasible in practice because of the low energy density of the stored air, this simple system configuration is a basic unit in any multi-stage system configurations. Understanding the dynamics of this elementary configuration provides a basis for further investigations. Additionally, the configuration should be a good example to technically demonstrate the capability of the proposed modelling framework in simulating the system and coupling the performance between the connected components.

Among different compressors, in addition to the longest history and various applications in compressor development, different from dynamic compressors (centrifugal and axial compressors) which usually achieve high-pressure ratios through a multi-stage configuration, a reciprocating compressor is capable of providing very high-pressure ratios in the single-stage because of its high internal volumetric ratio [15]. Using the reciprocating compressor in the selected single-stage compression, the advantageous high pressure ratio enables the system to have a wide range of stored temperature of particles in the PBTES. For example, the potential stored temperature can reach approximately 300 $^{o}$C if air from the atmosphere is pressurised to 10 bar adiabatically, and around 428 $^{o}$C if it is adiabatically compressed to 20 bar.

A radial turbine can be directly connected to a high-speed synchronous generator without any losses in mechanical transmission [16]. Compared to volumetric expanders, radial turbines usually allow higher power outputs through a single-stage configuration. Also, a single-stage radial turbine usually has better performance than a single-stage axial turbine, in small-scale applications.

PBTES is a combination of HEXs and thermal store, which uses direct-contact heat transfer between the compressed air and the TES particles in A-CAES. Compared to a system with indirect-contact HEXs, advantages of an A-CAES using PBTES include [6]: no thermal fluid requirement, low exergy loss because of the temperature stratification, high heat transfer coefficient, and potentially high-temperature heat storage.

Therefore, the A-CAES system with selected components is used

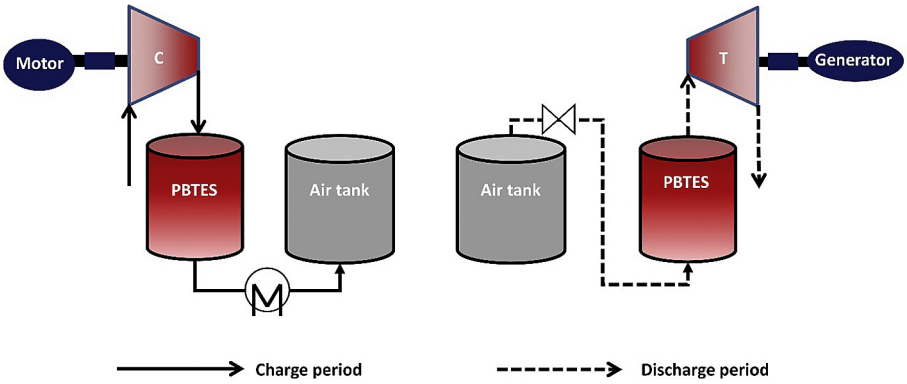


**Fig. 1.** Illustrated A-CAES using the PBTES with the single-stage compression and the single-stage expansion.

for developing the detailed cycle-to-cycle analysis.

## 3. Mathematical model for dynamic analysis

In order to simulate the system transient behaviours, models of components used in this study are introduced in this Section. The objective of this study is to link the time-variant performance at the system-level to the time-variant performance at the system-level. Because dynamics of each component in the system are complex in nature, in order to balance the computational cost, assumptions and simplifications are made in the models below.

### 3.1. Reciprocating compressor

The reciprocating compressor is typically driven by a motor, converting electricity to rotational motion of shaft, and pressurising air by a reciprocating piston. The model describing the behaviour of the reciprocating machine includes rotational motion of the shaft, reciprocating motion of the piston, periodic movement of valves, and flow of air through the cylinder. As shown in Fig. 2, in the single-stage reciprocating compressor, the torque generated by crankshaft drives a piston that moves in a reciprocating way between the top dead centre and the bottom dead centre, via the connecting rod.

The torque of compressor consists of two parts: one due to the air pressure variation in the cylinder, $f_p$, and the other one caused by the inertial force of the piston and rod, $f_m$. These torques can be presented as [17],

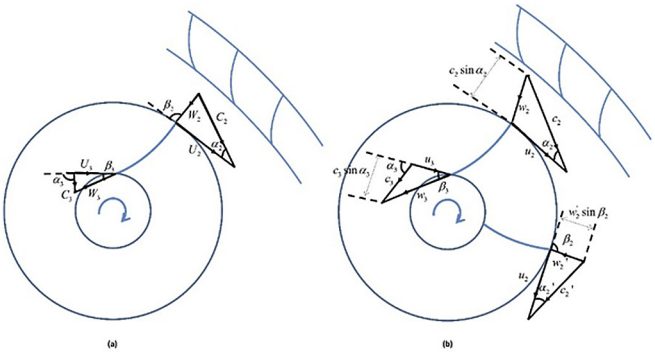

**Fig. 2.** Illustrated velocity triangles at inlet and outlet of the rotor in a radial turbine. The velocity triangles of the design operation is in (a) and the velocity triangles of the off-design operation is in (b).

$$f_p = 0.25\pi B^2 p_c\left(\sin\theta + \cos\theta\frac{r\sin\theta}{\sqrt{l^2 - r^2\sin^2\theta}}\right);$$
$$f_m = -m_c\frac{dv_p}{dt}\left(\sin\theta + \cos\theta\frac{r\sin\theta}{\sqrt{l^2 - r^2\sin^2\theta}}\right); \quad (1)$$

where $p_c$ is the pressure of air in the cylinder, $B$ is the bore diameter, $\theta$ is the shaft rotating angle, $r$ is the shaft radius, $l$ is the rod length, $v_p$ is the velocity of piston, and $m_c$ is the reciprocating mass which is [17].

$$m_c = m_p + 0.5m_r \quad (2)$$

where $m_p$ and $m_r$ are the piston mass and the rod mass respectively. Additionally, the reciprocating motion of piston can be modelled according to the evolution of the shaft. Thus, the velocity of piston is [17].

$$v_p = \omega r\left(\sin\theta + \cos\theta\frac{r\sin\theta}{\sqrt{l^2 - r^2\sin^2\theta}}\right) \quad (3)$$

where $\omega$ is the rotational speed.

Besides the mathematical models describing the motions of shaft, piston and rod, mass and energy flows of air are necessary to fully resolve the energy conversion between the mechanical rotation and the potential of air. It is assumed that the air in the cylinder is uniformly distributed, indicating that the model simulates the average air property. The friction losses and the mass leakage through the piston rings are neglected. The mass balance and energy balance are

$$\frac{dm}{dt} = \dot{m}_{in} - \dot{m}_{out} \quad (4)$$

$$\frac{d(mu)}{dt} = \dot{Q} - \dot{W} + \dot{m}_{in}h_{in} - \dot{m}_{out}h_{out} \quad (5)$$

where $u$ is the internal energy, $\dot{Q}$ is the heat transfer rate, $\dot{W}$ is the rate of work, $h$ is the enthalpy, $\dot{m}$ is the mass flow rate of air, and subscript *in* and *out* denote the property at the inlet and the outlet of a cylinder, respectively. Since internal energy can be presented as

$$u = h - pv = h - pV/m \quad (6)$$

where $V$ is the volume of the cylinder, $p$ is the air pressure. Substituting equation (6) into equation (5), energy equation can be rewritten,

$$\frac{d(mh)}{dt} = V\frac{dp}{dt} + \dot{m}_{in}h_{\text{in}} - \dot{m}_{out}h_{\text{out}} + \dot{Q} \tag{7}$$

Substituting equation (4) to equation (7), the equation changes to,

$$\frac{d(mh)}{dt} = c_pT\frac{dm}{dt} + mc_p\frac{dT}{dt} \tag{8}$$

where $c_p$ is the specific heat capacity, and $T$ is the air temperature. In addition, if the air is assumed to follow the ideal gas theory, it is,

$$pV = mRT \tag{9}$$

where $R$ is gas constant. Therefore, combining equations (7)–(9), the temperature variation of air can be obtained,

$$\frac{dT}{dt} = \frac{1}{mc_p}\left(V\frac{dp}{dt} + \dot{m}_{in}h_{\text{inflow}} + \dot{Q}\right) \tag{10}$$

where the inflow enthalpy $h_{\text{inflow}} = h_{in} - h$. The outflow enthalpy is zero, because the air at the outlet has the same enthalpy to the air in the cylinder based on the assumed uniformly distributed air in the cylinder.

Moreover, the pressure variation can be obtained by differentiating equation (9)

$$p\frac{dV}{dt} + V\frac{dp}{dt} = \frac{dm}{dt}RT + mR\frac{dT}{dt} \tag{11}$$

Substituting equations (4) and (10) into equation (11), the pressure variation is

$$\frac{dp}{dt} = \frac{1}{V}\left(\kappa RT_{in}\dot{m}_{in} - \kappa RT\dot{m}_{out} - \kappa p\frac{dV}{dt} + (\kappa - 1)\dot{Q}\right) \tag{12}$$

where $\kappa$ is the heat capacity ratio, and volume variation $dV/dt$ is determined by the geometric parameters and the velocity of piston,

$$\frac{dV}{dt} = 0.25\pi B^2 v_p \tag{13}$$

Heat transfer between the air in the cylinder to the walls in a reciprocating compressor is complex because of the time-variant heat transfer rate which is caused by the moving piston and the compressibility of air. Classical Newton law of cooling which assumes that heat flux is proportional to bulk gas-wall temperature difference no longer holds for simulating the in-cylinder heat transfer with a rotating piston [18]. A single and constant heat transfer coefficient is not sufficient to describe the convective heat transfer between the air in cylinder and the cylinder walls.

A number of works have been done to approximate this unsteady in-cylinder heat transfer. One attempt is to modify the Nusselt number correlations through the suitable Reynolds number over different stages of the moving piston and the air in cylinder. Adair et al. presented a corrected expression of the Nusselt number using Reynolds and Prandtl numbers, which correlated the time-averaged experimental data of instantaneous gas-to-wall heat transfer rates within 20% [19]. Disconzi et al. proposed a correlation of the Nusselt number with different fitted parameters and definitions for the Reynolds number over four processes of a cycle, namely suction, compression, expansion and exhaust [20]. The proposed correlations reasonably agreed with the CFD results in a number of quite different operating conditions [20]. Tuhovcak et al. reviewed these correlations and selected five correlations for comparing the effect of the correlation on compressor efficiency [21]. The comparison indicated similar trends of these correlations though discrepancies in values were found among the heat transfer models [21].

In addition to these correlations, works which particularly focused on simulating the transient heat transfer between the rapidly compressed and expanded gas to the surrounding walls have also been developed. Gas spring is an excellent simplification to study the losses due to this unsteady heat transfer between the gas and the cylinder walls while avoiding the complexities of gas inflow and outflow. Kornhauser and Smith derived the gas-to-walls heat transfer in a gas spring using complex temperature, heat flux, and the Nusselt number [18,22]. The imaginary part of the complex Nusselt number is caused by a phase difference between the heat flux next to the wall and the temperature difference between the bulk gas and the wall [18]. Mathie et al. proposed a framework to investigate the time-variant in-cylinder gas dynamics with a one-dimension unsteady conjugate heat conduction equation imposed by a suitable complex heat flux boundary from experiments in gas springs [23].

The main focus of this study is building up a system dynamic modelling framework which simulates cycle-to-cycle A-CAES system performance with the knowledge of time-dependent performance at the component-level. At the early stage, for simplicity, we used the corrections of the Nusselt number within the whole operating cycle of a reciprocating compressor from Ref. [20] to estimate the average heat transfer rates in the processes of suction, compression, expansion, and exhaust. It should be noted that the accuracy of the predicted average heat transfer rates significantly depends on the suitability of the fitted parameters and the chosen correlations. The unsteadiness of the heat transfer rates will be considered in future work with a more detailed model, such as the models in Ref. [23].

Therefore, with the corrected heat transfer coefficients over the four processes within a cycle [20], heat transfer rate between the air inside the cylinder and the walls is expressed as,

$$\dot{Q} = h_cA_c(T_w - T) \tag{14}$$

where $h_c$ is the corrected heat transfer coefficient, $A_c$ is the surface area of wall contacting with air in the cylinder, and $T_w$ is the wall temperature which is assumed to be uniformly distributed within the cylinder wall. An empirical correlation is selected to approximate the unsteady wall temperature, which is [15].

$$T_w = T_1 + \xi_w\frac{T_{2,s} - T_1}{2} \tag{15}$$

where $T_1$ is the air temperature during suction, $T_{2,s}$ is the compressed air temperature after an adiabatic process, $\xi_w$ is about 0.5 or lower if the cooling wall technique is applied [15].

The correlations to present the heat transfer in cylinder are in a general form [20],

$$Nu = \frac{h_c}{Bk} = a\text{Re}^b\text{Pr}^c \tag{16}$$

where $Nu$ is the Nusselt number, Re is the Reynolds number, and $k$ is the gas heat conductivity. $\text{Pr} = c_p\mu/k$ is the Prandtl number. $\mu$ is the viscosity. To account for the valves effect, Disconzi et al. divided the compression cycle into four consecutive processes, suction, compression, discharge and expansion, and derived different Reynolds number expressions and empirical constants [20]. The associated constants are listed in Table 1.

The mean velocity of the piston reciprocating move, $\overline{v_p}$, and the characteristic velocity for the Reynolds number during the suction and discharge processes, $v_c$, are [20].

**Table 1**
Reynolds number expressions and empirical constants for each process in compression cycle [20].

| Process | Reynolds number | Empirical constants |
|---|---|---|
| Compression | $\mathrm{Re} = \rho B\overline{v_p}/\mu$ | $a = 0.08; b = 0.8; c = 0.6$ |
| Discharge | $\mathrm{Re} = \rho B(\overline{v_p} + \overline{v_p}^{0.8} v_c^{0.2})/\mu$ | $a = 0.08; b = 0.8; c = 0.6$ |
| Expansion | $\mathrm{Re} = \rho B\overline{v_p}/\mu$ | $a = 0.12; b = 0.8; c = 0.6$ |
| Suction | $\mathrm{Re} = \rho B(\overline{v_p} + \overline{v_p}^{-0.4} v_c^{1.4})/\mu$ | $a = 0.08; b = 0.9; c = 0.6$ |

$$\begin{aligned} &\overline{v_p} = 2L\omega; \\ &v_c = \dot{m}\Big/(\rho A_{cr}) \end{aligned} \tag{17}$$

where $L$ is piston stroke, and $A_{cr}$ is cross-sectional area of the cylinder.

The flow through valves in a reciprocating machine is simplified that these valves are assumed to be on/off switches. Taking the suction valve as an example, if the force from the suction air is larger than the sum of the force from the air in the cylinder and the applied spring force, the valve opens. Otherwise, it is closed. The mass flow rate through the suction valve and the discharge valve are determined using isentropic compression flow approximation [24],

$$\begin{aligned} \dot{m}_{in} &= A_{in,eff} p_s \sqrt{\frac{2\kappa}{(\kappa-1)RT}} \sqrt{\left(\frac{p}{p_s}\right)^{2/\kappa} - \left(\frac{p}{p_s}\right)^{(\kappa+1)/\kappa}}; \\ \dot{m}_{out} &= A_{d,eff} p \sqrt{\frac{2\kappa}{(\kappa-1)RT}} \sqrt{\left(\frac{p_d}{p}\right)^{2/\kappa} - \left(\frac{p_d}{p}\right)^{(\kappa+1)/\kappa}} \end{aligned} \tag{18}$$

where $A_{in,eff}$ and $A_{d,eff}$ are the lumped effective area of the suction and the discharge plenum opening. The valve effective area are fitted with respect to the suction and discharge pressure.

### 3.2. Radial turbine

In a radial turbine, energy conversion can be approximately described by the Euler Equation of Turbomachines [25]. Different geometries and fluid conditions significantly affect the performance of the turbine. In a radial turbine used in CAES, compressed air enters turbine stator/rotor at one radius with one velocity and leaves at another radius with another velocity. Illustrated velocity triangles of the air at inlet and outlet of a stator-rotor stage are shown in Fig. 2 in which Fig. 2(a) are the velocity triangles in the design operation, and those in the off-design operations are shown in Fig. 2(b). In the design operation, air flows into the rotor according to the designed inlet angle. In contrast, in the off-design operations, vortices are generated due to the mismatch between the flow angle and the designed inlet angle, leading to an incidence loss. The turbine is considered as a purely resistive fluid flow component in which the accumulation of mass, momentum and energy inside the turbine flow path are neglected [26].

The changes in momentum of the air convert to the turbine's work, which drives the externally applied torque, namely the generator in the A-CAES. The specific work can be described as follows,

$$w_t = \Delta h = u_2 c_{w2} - u_3 c_{w3} \tag{19}$$

where $u$ and $c_w$ are tangential velocity of the rotor and the air, respectively. The tangential velocity of the rotor is dependent on the rotor size and the rotation speed, which is

$$u_2 = \frac{\pi N D_2}{60} \tag{20}$$

where $D$ is the diameter, $N$ is the rotational speed in rpm. The velocity of air at the inlet of the rotor is converted from the pressure of compressed air in the stator. Within the stator, the energy conversion from a pressure head to a velocity head. The air velocity at the outlet of the stator can be estimated based on the pressure drop through a nozzle,

$$c_2 = \sqrt{2(\Delta h_{1-2s} - \Delta h_{2loss})} \tag{21}$$

where $c$ is the absolute velocity, and $\Delta h_{2loss}$ is the enthalpy loss due to the friction in the stator. It can be approximated by Ref. [27],

$$\Delta h_{2loss} = \frac{1}{2}\xi_2 c_2^2 \tag{22}$$

in which $\xi_2$ is the enthalpy loss coefficient.

The simplified analysis above describes an averaged isentropic flow, which does not consider the incidence loss. The model only applies to the design operational conditions. However, turbines are operated in a wide range of conditions, turbine performance in partial-load conditions is also important. As shown in Fig. 2(b), a partial-load operation results in the incidence loss due to a sudden change of the flow. A simplified method was proposed by Wallace for estimating the incidence loss in an off-design operation based on energy conservation [28].

In the off-design operations, the sudden change of the air flow direction is accompanied by a formed shock, which dissipates the air kinetic energy to heat. Considering the formed shock wave, according to the study, the energy balance equation becomes [28].

$$C_p T_2 + \frac{c_2^2}{2} = C_p T_2' + \frac{c_2'^2}{2} + \left[c_2 \cos\alpha_2 - c_2 \sin\alpha_2 \frac{T_2'}{T_2} \cot\beta_2 - u_2\right] u_2 \tag{23}$$

where $T_2'$ and $c_2'$ are the varied temperature and velocity due to the sudden deflection of the flow. The continuity of the mass flow in radial direction is [28].

$$\frac{w_2' \sin\beta_2}{c_2 \sin\alpha_2} = \frac{T_2'}{T_2} \tag{24}$$

where $w'$ is the varied relative velocity. Based on equations (23) and (24), the changed temperature $T_2'$ due to the incidence loss can be obtained. Furthermore, the relative velocity of air at the outlet of the rotor is,

$$w_3 = w_2 + 2(\Delta h_{2-3s} - \Delta h_{3loss}) + u_3 - u_2 \tag{25}$$

where $\Delta h_{3loss} = \xi_3 w_3^2/2$ is the frictional loss within the rotor [27]. Additionally, considering all the energy losses, toque produced in the rotor can be obtained. The torque is composed of two parts, namely, that due to the sudden deflection of the flow entering the rotor, and that produced within the rotor passage. Therefore, the two torques are expressed as [28].

$$\tau_l = \frac{\left[c_2 \cos\alpha_2 - c_2 \sin\alpha_2 \frac{T_2'}{T_2} \cot\beta_2 - u_2\right] D_2}{2}; \tau_r = \frac{\left[c_2' \cos\alpha_2' + \frac{D_3}{D_2} c_3 \cos\alpha_3\right] D_2}{2} \quad (26)$$

where $\tau_s$ is the torque due to flow deflection and $\tau_r$ is the mechanical torque of the rotor. The isentropic efficiency of the turbine is

$$\eta_s = \frac{(\tau_s + \tau_r)\omega}{\Delta h_{13s}} = \frac{(\tau_s + \tau_r)}{\frac{K}{K-1} RT_1 \left[\left(\frac{p_3}{p_1}\right)^{\frac{\kappa-1}{\kappa}} - 1\right]} \frac{2\pi N}{60} \quad (27)$$

Due to the mass balance, an appropriate pressure $p_2$ needs to satisfy the conservation of energy as shown in equation (23) and the conservation of mass $\dot{m}_N = \dot{m}_R$, which are shown below [28],

$$\dot{m}_N = c_2 \sin\alpha_2 \pi D_2 b_2 \rho_1 \left(\frac{p_2}{p_1}\right)^{1/k}; \dot{m}_R = c_3 \sin\alpha_3 \pi D_3 b_3 \rho_2 \frac{T_2}{T_2'} \left(\frac{p_3}{p_2}\right)^{1/k} \quad (28)$$

Therefore, if the two mass flow rates are not equivalent, an iterative calculation has to be made to find the appropriate pressure ratios through the stator and rotor, until the mass balance is achieved.

### 3.3. Packed bed thermal energy storage

A schematic diagram of PBTES filling is shown in Fig. 3. The PBTES is assumed to be a vertical cylinder that has two ports for air inflow and outflow respectively. The PBTES is assumed to be packed using spherical particles filled with heat storage materials. Compressed air from the compressors flows into the PBTES for storing the compression heat and then re-heating up the air during the discharge.

The considered heat transfer between air and particles in the PBTES includes both convection and conduction. To reduce the computational burden and simplify the model, some assumptions are employed in simulating the PBTES [9]: 1) The temperature of thermal particles is averaged along the radial direction within the PBTES tank; 2) Uniform porosity is used in the modelling; 3) No flow accumulation in the PBTES that constant average mass flow rate is assumed from inlet to outlet; 4) Every single particle has uniform temperature that temperature variation in the particle is not resolved. For a PCM-filled particle, the temperature is solved at the macroscopic scale and the pore-scale variations are not modelled. Thermal resistance of the encapsulated layer for a PCM filled particle is not considered.

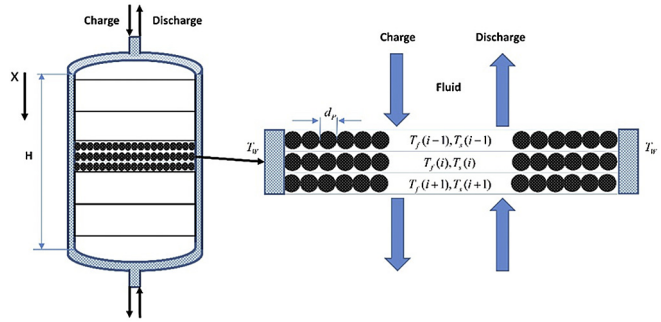


**Fig. 3.** Schematic diagram of a PBTES with PCM fillings.

With these assumptions, therefore, an unsteady energy conversion model is developed to present the heat transfer between compressed air and particles within the PBTES. The model includes two governing equations. For the compressed air, the simplified one-dimension unsteady energy conservation equation is [9],

$$\varepsilon\rho_f c_{p,f}\left(\frac{\partial T_f}{\partial t} + u_f \frac{\partial T_f}{\partial x}\right) = \varepsilon k_f \frac{\partial^2 T_f}{\partial x^2} + h_{fs}\left(T_s - T_f\right) + h_W\left(T_W - T_f\right) \quad (29)$$

where $\varepsilon$ is the porosity of the filled particles, $\rho_f$, $c_{p,f}$ and $k_f$ are density, heat capacity and thermal conductivity of the compressed air respectively. $u_f$ is the velocity of the compressed air. $T_f$ and $T_s$ are the temperature of the air and the particles in the PBTES, respectively. $T_W$ is the temperature of the tank wall. $h_{fs}$ is the heat transfer coefficient between the air and the particles, and $h_W$ is the heat transfer coefficient through the tank wall.

In addition to the governing equation of the working fluid, heat transfer of the particles in the PBTES without the phase change is presented as [9].

$$(1-\varepsilon)\rho_s c_{p,s} \frac{\partial T_s}{\partial t} = (1-\varepsilon) k_s \frac{\partial^2 T_s}{\partial x^2} + h_{fs}\left(T_f - T_s\right) \quad (30)$$

where $\rho_s$, $c_{p,s}$ and $k_s$ are density, heat capacity and thermal conductivity of the particles respectively.

The filling of the particles usually consists of sensible heat storage materials and latent heat storage materials. The sensible heat storage material stores energy in terms of the temperature variation of the material. In contrast to the sensible heat energy storage, the latent heat energy storage material absorbs or releases energy using the phenomenon of the isothermal phase changing. In this study, the thermal particles are assumed to allow the volume variation of PCMs due to the phase transition. Therefore, the porosity and the volume of particles occupied in PBTES are considered as constant during the phase-changing period [8].

Thermodynamic properties of latent heat storage materials change significantly due to the phase variation. Also, the heat of fusion is released during latent heat transfer, which needs to be specifically considered in the latent heat storage. Thus, the enthalpy method is used [8]. The method employs variable thermodynamic properties of the material to simulate the significantly changed heat transfer due to the phase change. Thus, thermodynamic properties of a PCM are defined among three stages [8]. The three stages, solid phase stage, phase changing stage, and liquid phase stage, are differentiated by the material's temperature.

In the solid phase stage,

$$T_s < T_{m1} : c_{P,s} = c_{P,s}^{PCM}; k_s = k_s^{PCM} \quad (31)$$

During the phase changing stage, the latent heat is accounted by spreading the energy over a very small temperature difference. In the phase changing period,

$$T_{m1} \le T_s < T_{m2} : c_{P,s} = \frac{c_{P,s}^{PCM} + c_{P,l}^{PCM}}{2} + \frac{\gamma_l}{T_{m1} - T_{m2}}; k_s = \frac{k_s^{PCM} + k_l^{PCM}}{2} \quad (32)$$

In the stage of liquid phase of PCM,

$$T_s \geq T_{m2} : c_{P,s} = c_{P,l}^{PCM}; k_s = k_l^{PCM} \tag{33}$$

where $c_{P,s}^{PCM}$ and $k_s^{PCM}$ are heat capacity and thermal conductivity of the PCM in the solid phase, $c_{P,l}^{PCM}$ and $k_l^{PCM}$ are those of the PCM in the liquid phase. $\gamma_l$ is specific latent heat of the PCM. $T_{m1}$ and $T_{m2}$ are the two limiting temperature ends of the PCM phase changing process.

To solve Equations (29) and (30), boundary conditions and initial conditions need to be configured, in which initial conditions are

$$T_f(t=0) = T_{air,in}; T_s(t=0) = T_{s,store} \tag{34}$$

where $T_{air,in}$ is the temperature of the compressed air flowing into the PBTES, and $T_{s,store}$ is the temperature of the particles in the PBTES at the beginning of the charge or discharge period. For the boundary conditions,

$$\begin{aligned} &\text{Charge}: T_f(x=0) = T_s(x=0) = T_{air,in}; \frac{\partial T_f(x=H)}{\partial x} = \frac{\partial T_s(x=H)}{\partial x} = 0 \\ &\text{Discharge}: T_f(x=H) = T_s(x=H) = T_{air,in}; \frac{\partial T_f(x=0)}{\partial x} = \frac{\partial T_s(x=0)}{\partial x} = 0 \end{aligned} \tag{35}$$

where $x$ is the coordinate along the flow direction as shown in Fig. 3, $H$ is height of the PBTES. The heat transfer coefficient between the compressed air and the particles, $h_{fs}$, and the heat transfer coefficient presenting heat dissipation through layers of the insulation and the tank wall with the ambience, $h_W$, are estimated using empirical correlations. Yang et al. presented several correlations of the Nusselt Number in the PBTES modelling [29]. The correlation is based on a numerical model in which several assumptions were made [29]: 1) the time-dependent air flow and temperature of central packed channel only change along the flow direction; 2) Constant thermal properties of the air and the particles in the PBTES; 3) No local thermal equilibrium between the air flow and the particles. By comparing simulations with the measured outlet air temperature, they obtained the heat transfer correlations [29]. Peng et al. selected one of them and used it to investigate a similar PBTES design with encapsulated PCMs [9]. The validation in the work indicated acceptable agreement between the simulation and the experimental results [9]. Therefore, for simplicity, this study employed the correlation. It should note that the framework can adopt any other correlations of the Nusselt number if any improvement of predicting the heat transfer rate is needed. Thus, the heat transfer coefficient, $h_{fs}$, is calculated using [9,29].

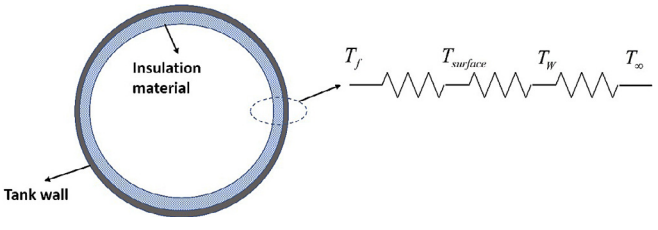


**Fig. 4.** Illustrated thermal resistance model of heat transfer between compressed air and ambience through wall and insulation.

$$Nu_f = \frac{h_{fs} d_p}{k_f} = 2.2 + 0.56 \mathrm{Pr}_f^{1/3} \mathrm{Re}_p^{0.65} \tag{36}$$

where

$$\mathrm{Pr}_f = \frac{c_{p,f}\mu_f}{k_f}; \mathrm{Re}_p = \frac{\rho_f d_p \varepsilon u_f}{\mu_f} \tag{37}$$

This study utilises an overall heat transfer coefficient to estimate the heat transfer through the insulation material and the tank wall to the ambience in the radial direction. As shown in Fig. 4, the radial heat transfer problem is simulated using thermal resistance model. From the fluid inside the tank to the ambience, there are three thermal resistance layers. For simplicity, it is assumed that temperature of the tank wall is equivalent to that of the ambience, namely $T_w = T_\infty$.

The energy balance can be obtained based on the heat flux,

$$\frac{2\pi H k_{insulation}}{\ln(D_{outer}/D_{inner})}\left(T_f - T_{surface}\right) = h_{wall}\pi D_{outer} H\left(T_{surface} - T_\infty\right) \tag{38}$$

where $k_{insulation}$ is heat conductivity of the insulation material, and $h_{wall}$ is natural heat transfer coefficient of the tank wall, which can be obtained using [8,9].

$$\begin{aligned} Nu(x) &= \left[\frac{7Gr(x)\mathrm{Pr}_f^2}{100 + 105\mathrm{Pr}_f}\right]^{1/4} + \frac{4\left(272 + 315\mathrm{Pr}_f\right)}{35\left(64 + 63\mathrm{Pr}_f\right)}\frac{x}{D_{outer}} = \frac{h_{wall}}{k_f} \\ Gr(x) &= \frac{g\left(T_{surface} - T_w\right)x^3}{\nu^2\left(T_{surface} + T_w\right)} \end{aligned} \tag{39}$$

Therefore, the overall heat transfer coefficient for heat dissipation to the ambience is given by Ref. [30].

$$\frac{1}{h_l} = \frac{D_{outer}\ln(D_{outer}/D_{inner})}{2k_{insulation}} + \frac{1}{h_{wall}} \tag{40}$$

Consider the volumetric effect, the overall volumetric heat transfer is [31].

$$h_w = h_l\frac{4\pi D_{outer}}{\pi D_{outer}^2} = \frac{4h_l}{D_{outer}} \tag{41}$$

To estimate pressure drop of the compressed air, in addition, frictional factor in the PBTES can be calculated using Ergun equation [6]. Considering a thermal buoyancy effect, pressure drop of the air in the PBTES using spherical capsules can be presented as [32,33].

$$\Delta p = L\left(\frac{(1-\varepsilon)^2}{\varepsilon^3}\frac{150\mu_f}{\psi^2 d_p^2}u_f + \frac{1-\varepsilon}{\varepsilon^3}\frac{1.75\rho_f}{\psi d_p}u_f^2\right) + \rho_f g L\frac{\Delta T_f}{T_f} \quad (42)$$

where $\psi = 6V_p/(A_p d_p)$ considers the sphericity of the particles with unity for a sphere, $V_p$ and $A_p$ are volume and surface area of a single particle. The product of $\psi$ and $d_p$ is the equivalent spherical particle diameter.

### 3.4. Air storage

Air tank is a constant volume (isochoric) storage in which the compressed air is stored. There is neither source nor sink in the tank. However, because of the compressibility of the air, the density of the air in the tank changes during both the charge and discharge periods of the A-CAES. In addition, the temperature of the air is also varied. Therefore, based on the mass and energy conservations, the governing equations of a constant volume air tank/storage are [34],

$$\begin{aligned}\frac{d\rho}{dt} &= \frac{\dot{m}_{in,as} - \dot{m}_{out,as}}{V_{as}} \\ \frac{d(mU)}{dt} &= \left(\dot{m}_{in,as}h_{in} - \dot{m}_{out,as}h_{out}\right) - h_{W,as}A_{as}(T_{as} - T_W)\end{aligned} \quad (43)$$

where subscript *as* denotes air storage. Using ideal gas theory and the first law of thermodynamics, energy equation can be rewritten as,

$$\rho c_P\frac{dT}{dt} + \frac{m_{in,as}}{V_{as}}c_p(T_{as} - T_{in}) - \frac{dp}{dt} + \frac{h_{W,as}A_{as}}{V_{as}}(T_{as} - T_W) = 0 \quad (44)$$

Using the lumped volumetric heat transfer coefficient from Ref. [34], an experimental correlation is fitted,

$$h_{eff} = \frac{h_{W,as}A_{as}}{V_{as}} = a + b\left|m_{in,a} - m_{out,a}\right|^{0.8} \quad (45)$$

where $a$ and $b$ represent the heat transfer coefficient caused by natural convection and forced convection in the storage. $h_{eff}$ is the lumped volumetric heat transfer coefficient.

### 3.5. Throttling valve

Mechanism of a throttling valve is to manage fluid flow by constriction or obstruction. The process of throttling is assumed to be isenthalpic, which is

$$dh = 0 \quad (46)$$

In the model, *CoolProp* is used for considering the Joule-Thompson effect and considered the temperature reduction due to air expansion.

### 3.6. System performance

The cycle efficiency of the system is defined as the ratio of energy output to the energy input. In this study, without considering the energy conversion loss between mechanical energy of compressor/turbine and electrical energy of motor/generator, the cycle efficiency of the system is

$$\eta = \frac{W_t}{W_c} \quad (47)$$

where $W_t$ is the work generated by the turbine and $W_c$ is the work consumed by the compressor.

In order to analyse the varied energy stored with the evolving cycles, heat stored in the PBTES is presented by the internal energy variations of the thermal particles, which is

$$E_{TES} = \int\left[V_{TES}(1-\varepsilon)\rho_s c_{p,s}\frac{\partial T_s}{\partial t}\right]_i dt \quad (48)$$

where $V_{TES}$ is the volume of the PBTES tank, and $E_{TES}$ presents thermal energy stored in the PBTES.

To evaluate the varied energy storage in terms of the compressed air, exergy stored of the compressed air storage (CAS) is

$$B_{CAS} = \dot{m}\left[c_p(T - T_0) - T_0\left(c_p\ln\frac{T}{T_0} - R\ln\frac{P}{P_0}\right)\right] \quad (49)$$

where $B_{CAS}$ is the exergy stored in the CAS, $T_0$ and $P_0$ are the reference (environment) temperature and pressure.

### 3.7. Dynamic modelling framework

Therefore, using the mathematical models of reciprocating compressor, radial turbine, PBTES, and air storage, dynamic modelling of the assembled A-CAES system can be carried out. Although models of some components derived above are based on ideal gas theory, the system model incorporates the variable air thermodynamic properties for estimating the real gas effect. Since the thermodynamic properties of air depend on the air pressure and temperature, in the A-CAES system modelling, *CoolProp* is used to estimate the variable thermodynamic properties of the compressed air [35]. Density, heat capacity, viscosity and thermal conductivity of the compressed air are calculated based on its pressure and temperature at each time-step, namely, $c_{p,f} = c_{p,f}(P_f, T_f)$, $\mu_f = \mu_f(P_f, T_f)$ and $k_f = k_f(P_f, T_f)$.

A flowchart of the system dynamic modelling framework is illustrated in Fig. 5. Because of the fast mechanical response of the shaft, it is assumed that constant rotational speed of compressor and turbine is maintained through well-developed controllers. The dynamic modelling framework is implemented in MATLAB software. Mathematical models of all the components are implemented using MATLAB scripting and the system is assembled in SIMULINK to investigate the system dynamic behaviours. The assembled ordinary differential equations (ODE) are solved using the ODE solvers in MATLAB.

Before running the simulation, parameters are initialised. At each time step, on the basis of the mathematical models of components described above, derivatives of key variables including pressure, temperature, mass flow rate of compressed air, and temperature of TES particles are calculated. The obtained derivatives are used to update these variables for the next time step by using time integration algorithm. The loop is repeated to simulate the time-dependent behaviour of both the components and system until the stopping time is reached. During the dynamic simulation, thermodynamic properties of both the compressed air and the TES particles are updated based on current temperature and pressure calculated at the end of each time step.

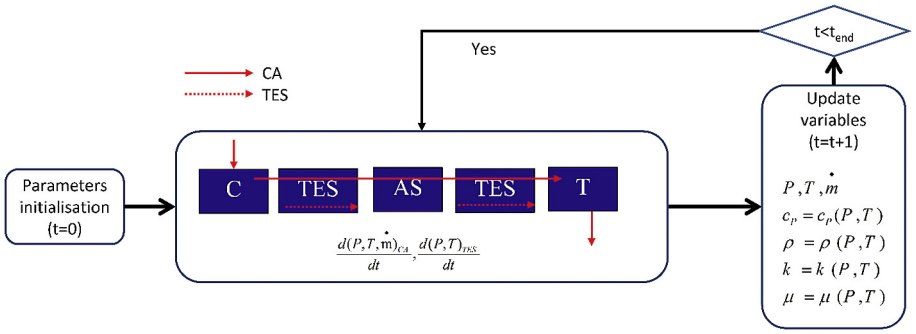


**Fig. 5.** Flowchart of dynamic modelling framework. C is short for the compressor. AS is short for the air storage tank. T is short for the turbine.

## 4. Validation of the component level mathematical models in the dynamic modelling framework

Before carrying out a dynamic modelling of the A-CAES system, the component level mathematical models of main components introduced above are validated by using experimental data from published literature. The parameters used in validations are listed in Table 2.

To validate the mathematical model of reciprocating compressor, isentropic efficiency and discharge temperature are compared with experimental data from Ref. [15]. Results of simulation and experiments from the literature are shown in Table 3. The results include five steady operations with different pressure ratios. In the simulation, the wall temperature of the cylinder is assumed to be constant but different in these five operations. Temperatures of cylinder wall are set according to the measured data in Ref. [15] for each simulation case. Because of the simple switch-like approximation of the valve model, oscillations of both air performance exist in the suction and discharge processes. The simulation results are average data of 20 steady-state cycles in each of the five operations. Through the comparisons, it indicated the capability of the component level model used in this study to approximate the performance of the reciprocating compressor with high accuracy. The compressor used in the validation is a small-scale machine whose operation is more close to the assumed conditions, so the comparison indicated the high accuracy of the model. With the increase of the compressor's size, the unsteadiness and non-uniformity of the air flow and temperature fields will affect the performance of the compressor more significantly.

In addition, comparisons between the simulated results using the radial turbine model and PBTES model to the experimetnal data are plotted in Figs. 6 and 7 respectively. According to simulated isentropic efficiency as shown in Fig. 6, the mean-line model of radial turbine is demonstrated to be capable of predicting the performance map in both design and off-design operations. Results plotted in Fig. 7 also indicates the capability of the PBTES model to present both the sensible and latent heat storage reservoirs. The simulated transient temperature profiles of the TES particles using parameters from Refs. [36,37] are compared with the experimental data, which are shown in Fig. 7(a) and (b) respectively. The results reasonably agree with the time-dependent variations of the experimental data. Although there are slight deviations between the simulated data of the PCM filling PBTES and the experimental data, the tendency of the changing transient temperature are captured by the modelling. The small deviations might be caused by the inaccuracy of the correlations, which were discussed in Ref. [9].

Moreover, for validation of the air storage modelling, testing data from the Huntorf plant is used. A variable mass flow rate of the discharging air from the trial operational data [34,38], as shown in Fig. 8(a), is used. The pressure and temperature variations during the discharge are presented in Fig. 8(b) and (c), respectively. The

**Table 2**
Parameters used in the validation of reciprocating compressor, radial turbine and PCM filling PBTES [15] [39] [36,40] [37] [34,38].

| Parameter | Value |
|---|---|
| Reciprocating compressor [15] | |
| Bore, m | 0.0762 |
| Stroke, m | 0.0635 |
| Clearance factor, | 4.5% |
| Crank rod length, m | 0.119 |
| Swept volume, $m^3$ | $5.792 \times 10^{-4}$ |
| Rotational speed, rpm | 938 |
| Radial turbine [39] | |
| Rotor inlet diameter, m | 0.1164 |
| Rotor outlet mean diameter, m | 0.0520 |
| Rotor inlet width, m | 0.0063 |
| Rotor outlet width, m | 0.0216 |
| Rotor outlet angle, degree | 77.6 |
| Nozzle outlet angle, degree | 57.4 |
| PBTES with solid TES particle filling [36,40] | |
| TES solid material | Rock |
| Working fluid | Air |
| Charging temperature, | 823 |
| Ambient temperature, K | 293 |
| Mass flow rate, kg/s | 0.004 |
| Height, m | 1.2 |
| Diameter, m | 0.148 |
| Particle diameter, m | 0.02 |
| Porosity | 0.4 |
| Heat capacity of solid, $J/(kg \cdot K)$ | 1068 |
| Density, $kg/m^3$ | 2680 |
| Heat conductivity, $W/(m \cdot K)$ | 2.5 |
| PBTES with PCM TES particle filling [37] | |
| TES PCM material | Coarser-GR50 |
| Working fluid | Air |
| Charge temperature, K | 338 |
| Ambient temperature, K | 293 |
| Mass flow rate, l/min | 450 |
| Height, m | 0.2 |
| Diameter, m | 0.2 |
| Particle diameter, m | $1.64 \times 10^{-3}$ |
| Porosity | 0.486 |
| Heat capacity of solid phase, $J/(kg \cdot K)$ | 1448.6 |
| Heat capacity of liquid phase, $J/(kg \cdot K)$ | 1735.7 |
| Specific latent heat, $J/kg$ | 54,739 |
| Melting temperature, $K$ | 323 |
| Heat conductivity, $W/(m \cdot K)$ | 0.2 |
| Parameters of carven in Huntorf plant [34,38] | |
| Volume of cavern, $m^3$ | 300,000 |
| Maximum operating pressure, bar | 72 |
| Minimum operating pressure, bar | 10 |
| Cavern wall temperature, K | 323 |
| Initial temperature of air during discharge, K | 306 |
| Mass flow rate of air during discharge, kg/s | 417 |

**Table 3**
Comparison of results of reciprocating compressor between simulation and experimental data from Ref. [15].

| Pressure bar | Average steady-state efficiency | | | Average steady-state discharge temperature, K | | |
|---|---|---|---|---|---|---|
| | Simulation | Experiment [15] | Relative difference | Simulation | Experiment [15] | Relative difference |
| 4.71 | 54.8% | 55.89% | 1.88% | 583 | 594 | 1.85% |
| 5.36 | 54.6% | 56.79% | 3.79% | 613 | 612 | 0.16% |
| 6.31 | 56.2% | 57.00% | 1.47% | 641 | 640 | 0.16% |
| 6.85 | 55.4% | 56.69% | 2.22% | 665 | 664 | 0.15% |
| 7.93 | 56.8% | 56.79% | 0.05% | 690 | 682 | 1.17% |

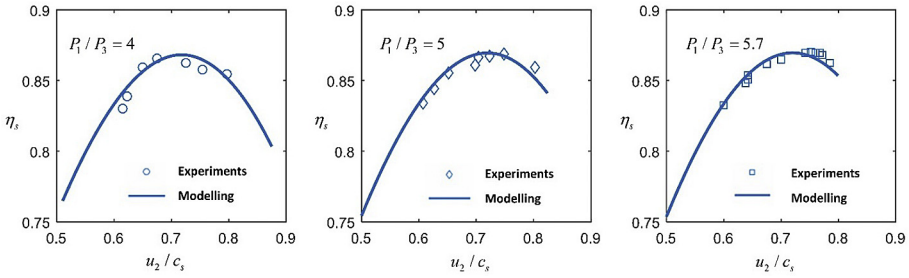


**Fig. 6.** Comparison of results of radial turbine between simulation and experimental data from Ref. [39].

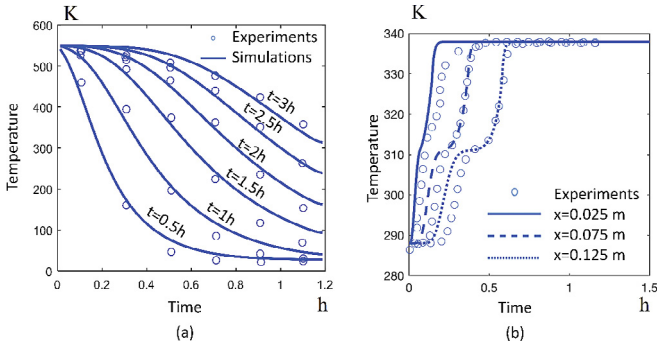


**Fig. 7.** Comparison of results of PBTES with solid filling [36,40] and PCM filling [37] between simulation and experimental data.

modelling results closely agree with the experimental data. Therefore, these component level mathematical models are employed to study the system performance.

## 5. Dynamic modelling of the A-CAES system

A case study of the selected A-CAES system is developed and presented in this section. Parameters of the reciprocating compressor, the radial turbine, the PBTES and the air storage used in this study are listed in Table 4. The regulated pressure is selected as 4 bar after the throttle valve. In the small scale A-CAES system, a reciprocating compressor with the aspect ratio (stoke/diameter) is 0.25 and clearance ratio is 0.05 is selected [41]. A set of geometric parameters of the radial turbine are preliminary designed for the simulation. Based on the model, isentropic efficiency of the radial turbine is approximately 82.7% with the inlet temperature 400 °C and inlet pressure 4 bar of air. Because optimal designs of these machines are beyond the scope of this study, these parameters of both the compressor and radial turbine are utilised in the early stage investigations. Volume of the air storage tank is 200 $m^3$. Fitted heat transfer coefficient of the air tank is obtained using experimental data in Ref. [5]. Parameters of the rock and the selected PCM material used in simulations are listed in Table 5. The height/diameter ratio of the PBTES is set as 5.

In order to resolve the dynamics of each component in the system, the time-step of the ODE solver needs to be properly set. Particularly, the reciprocating compressor has a periodic cycle-based operation in which the time of every cycle is usually very short because of the fast rotating speed. In this system, the piston of the compressor rotates at 800 rpm, i.e. a full revolution lasts about 75 ms. In order to fully resolve the dynamic performance of the reciprocating compressor, a fixed time-step 0.2 ms was used in the ODE solver.

A typical daily-cycle operation of the A-CAES system is composed of a charging period, an idle fully-charged period, a discharging period, and another idle empty period. This study utilises the air pressure in the storage tank as the criterion to determine the system operation. The studied cycle is shown in Fig. 9. The charging period (A-B) starts at the minimum air pressure

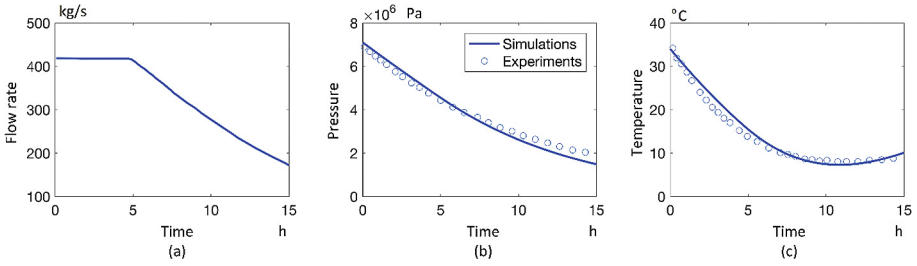


**Fig. 8.** Validation of air storage modelling with experimental data from Huntorf plant [34,38].

**Table 4**
Parameters of components.

| Parameters | Value |
|---|---|
| *Reciprocating compressor* | |
| Rotational speed, rpm | 800 |
| Diameter, m | 0.5 |
| Stroke length, m | 0.125 |
| Aspect ratio (stoke/diameter) | 0.25 |
| Clearance volume, $m^3$ | 0.01 |
| *Radial turbine* | |
| Rotational speed, rpm | 50,000 |
| Rotor inlet diameter, m | 0.1883 |
| Rotor outlet mean diameter, m | 0.0667 |
| Rotor inlet width, m | 0.0066 |
| Rotor outlet width, m | 0.0225 |
| Rotor outlet angle, degree | 77 |
| Nozzle outlet angle, degree | 56.1 |
| *PBTES* | |
| Height, m | 6 |
| Diameter, m | 1.2 |
| Particle diameter, m | 0.02 |
| Porosity | 0.4 |
| *Air storage* | |
| Volume, $m^3$ | 200 |
| *Operational parameters* | |
| Minimum stored pressure, bar | 4 |
| Ambient temperature, K | 298 |

in the storage tank and ends at the maximum air pressure. A 10-h idle storage time (B-C) after the fully-charged. Then, in the discharging period (C-D), the system generates the specific power outputs until the air pressure in the storage tank reduces to the minimum value. For illustrating the realistic operation, system discharging subject to a specific load/demand flowing is considered. With different inlet temperature, a given power profile is predefined for the A-CAES system to follow, which is shown in Table 6. Finally, another idle empty period (D-E) achieves the daily operation cycle. It is important to point out that the proposed models and associated analysis can be readily extended to deal with other operational strategies of the system.

At the system level, the two main components influencing energy storage capacity and system dynamics are the storage tank and the heat storage vessels, in which two types of energy are stored in both the compressed air and the particles. The simulated results of the exergy stored in CAS and the energy stored in TES are plotted in Fig. 10. Results of both the A-CAES systems with the selected sensible heat storage, in Fig. 10(a) and (b), and the system with the selected latent heat storage, in Fig. 10(c) and (d), are shown respectively.

As shown in Fig. 10(a) and (c), regulated profiles of exergy stored in CAS are found in both the systems with sensible and latent heat storage. These are the results of the utilised operational strategies which minimise the fluctuations of the energy storage in terms of the compressed air. A constant inlet air temperature is maintained by the HEX in front of the air storage tank, and the air pressure variation in the tank is controlled at each cycle. Moreover, in a single-cycle, due to the constant volume of the CAS, operational conditions of the components associated with the charging process are influenced. With the air inflowing to the storage tank, the pressure in the tank keeps increasing. Because of the negligible

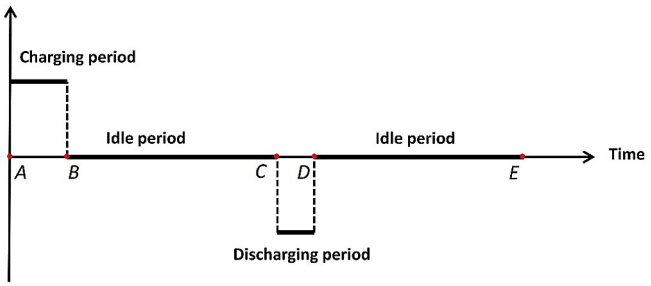


**Fig. 9.** Illustration of the single-cycle of the system operation.

**Table 6**
Predefined power output profile of the turbine subject to the inlet air temperature.

| Inlet air temperature of the turbine | Predefined power output, kW |
|---|---|
| $T_{inlet} \leq 400$ K | 60 |
| 400 K $< T_{inlet} \leq 450$ K | 70 |
| $T_{inlet} > 450$ K | 80 |

pressure losses through the pipes and the thermal stores, the outlet pressure of the compressor follows the tendency of the air pressure in the storage tank, which leads to a varied operational condition of the compressor. The operations of the compressor are shown in Fig. 11 in which the outlet pressure, outlet temperature, and mass flow rate are included.

Caused by the increased pressure ratio, air temperature at the compressor outlet increases rapidly with respect to the progress of the system charging. As shown in Fig. 11(b), the temperature increases from about 450 K at the beginning of the charging to more than 700 K when the air pressure reaches the maximum value in the storage tank. In addition, the increased pressure ratio of the compressor decreases the suction/discharge valves opening periods, resulting in the reduction of the mass flow rate when the system charging evolves. As shown in Fig. 11(c), the mass flow rate reduces from about 0.35 kg/s to less than 0.24 kg/s at the end of the system charging.

Different from the regulated energy storage in terms of the compressed air, energy stored in the TES vessel varies with respect to the evolving system cycles. As shown in Fig. 10, using the initial state as a reference (ambient temperature of the TES particles), the energy stored in the PBTES keeps increasing at a decreasing rate, and gradually reaches a steady state. These time-dependent cycle-to-cycle operations are caused by the mismatch between the TES full-discharging and the CAS full-discharging. In the first several cycles, the full-discharge of the TES cannot be achieved when the energy storage in the CAS is fully discharged. In these cycles, the temperature of the TES particles after the discharging cannot decrease to the initial state of those at the beginning of the system discharging. In other words, thermal energy is accumulating in the PBTES vessel with the system cycle evolving. However, the accumulating rate decreases to zero gradually when the steady-state is achieved.

Moreover, as indicated by Fig. 10(b) and (d), the sensible heat thermal storage reaches the steady state after about 20 cycles, but the selected latent heat storage needs about 70 cycles. Because the

**Table 5**
Parameters of solid particle and PCM particle in PBTES [42] [43].

| TES particle | Density kg/$m^3$ | Specific heat capacity J/$(kg \cdot K)$ | Thermal conductivity W/$(m \cdot K)$ | Melting temperature K | Heat of fusion kJ/kg |
|---|---|---|---|---|---|
| Rock [42] | 2500 | 830 | 5.69 | N/A | N/A |
| $NaNO_3$ [43] | 2260 | 1820 | 0.5 | ~583 | 172 |

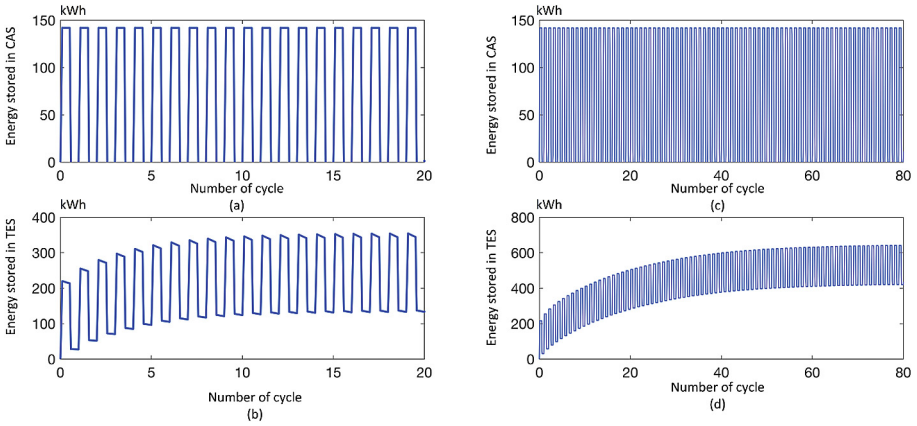


**Fig. 10.** Variations of exergy stored in CAS and energy stored in TES.

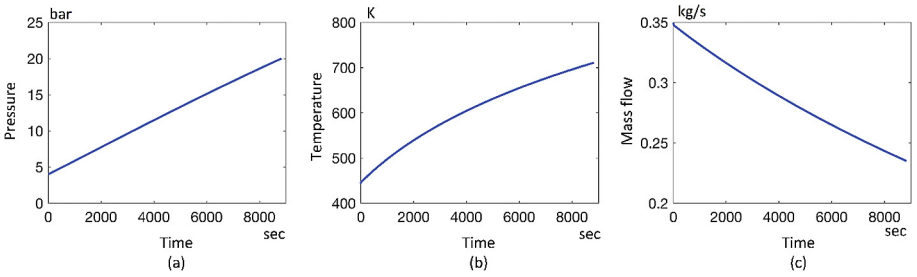


**Fig. 11.** Operational conditions of the compressor.

compression heat carried by the compressed air is restricted by the regulated durations of the system charging/discharging, heat gained and released by the PBTES are finite in every daily cycle. Due to the large thermal inertia and low response which are caused by the considerable heat of fusion during phase change and the low thermal conductivity, the PCM-filled PBTES requires more time to spread the heat through the whole tank.

Additionally, due to the high density of latent heat storage, a smaller size of the PCM-filled PBTES is allowed to achieve a similar heat storage capacity in the steady-state cycle compared to that with the sensible heat storage. Energy profile of a reduced size of PBTES with the selected PCM is plotted in Fig. 12 in which the sensible PBTES is also included for comparison. The height and diameter of the PCM-filled PBTES decrease to 4.55 m and 0.91 m, which agreees with the same height-diameter ratio as the PBTES vessel used in all simulations. As indicated by Fig. 12, the volume of the small-size PCM-filled PBTES is significantly reduced compared to the one as shown in Fig. 11(d), but the small PBTES has a relatively similar energy storage variations profile to the one of the rock-filled PBTES. The volume of the small PBTES vessel is only 43.5% of volume of the PBTES vessel with 6 m height. The containment cost of the paired pressure vessel is proportional to the product of pressure and internal volume of the heat reservoir [44]. The cost of containment per unit volume of the thermal store is very high because of the high pressure ratios required in CAES systems. So the volume reduction due to the high energy density of latent heat storage in an A-CAES will lead to considerable containment cost decrease.

The temperature profiles of the PBTES vessels whose height is 6 m are plotted in Fig. 13, in which the profiles are the particles' temperature at the end of system charging and discharging. The temperature profiles of the sensible heat storage are plotted in Fig. 13(a) and (b), and the profiles of the latent heat storage are plotted in Fig. 13(c) and (d). As indicated by Fig. 13, in both heat

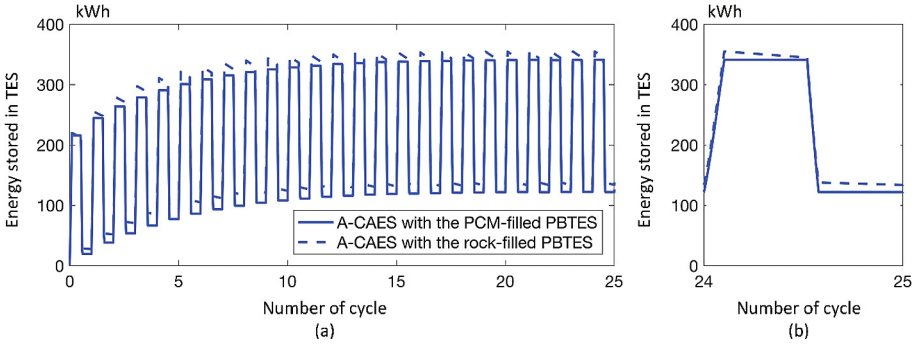


**Fig. 12.** Variations of energy stored in the TES.

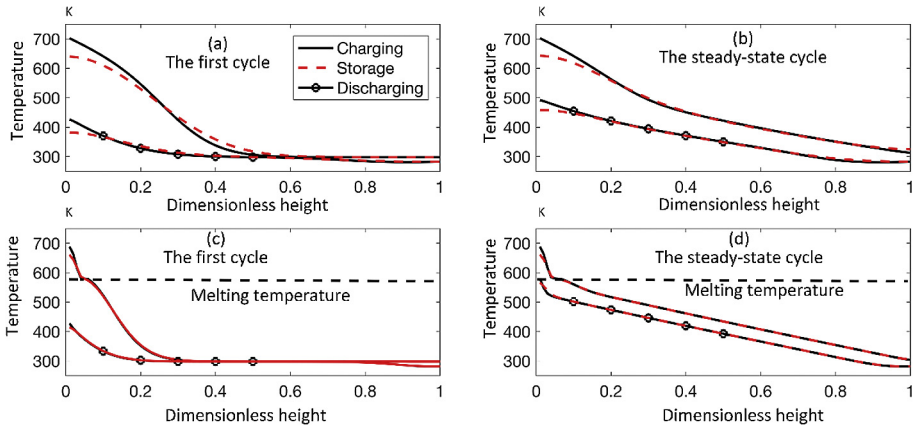


**Fig. 13.** Temperature profiles of the particles in the PBTES at the first cycle and steady-state cycle. The plotted profiles are the particles' temperature profiles at the end of the charging, storage, and discharging periods. The results of the rock-filled PBTES are plotted in (a) and (b). The results of the PCM-filled PBTES are plotted in (c) and (d).

storage systems, higher degree of the temperature stratification of the TES particles is achieved in the PBTES vessel at the steady-state cycle. These more evenly stratified temperature profiles minimise the temperature difference between the air and the particles, which leads to the reduction of heat transfer loss. Compared to the first cycle, additionally, the TES particles with the higher degree of the temperature stratification at the steady-state also reduce the exergy loss between the particles.

Furthermore, within an operational cycle, as shown in Fig. 13, temperature profiles of the PBTES are also different between the sensible and latent heat storages. Due to the high thermal conductivity of the rock, larger exergy losses occurred during the storage periods. The degree of temperature stratification of the rock particles decreases after storage periods in the first cycle as shown in Fig. 13(a). With improved temperature stratification in the steady-state cycle as shown in Fig. 13(b), degrade of the stratification mitigates but exergy losses of the particles with high temperature still occur. In contrast, as shown in Fig. 13(c) and (d), negligible deviations of the temperature profiles occurred after the storage periods in the selected PCM filled PBTES.

Because of significantly enhanced energy storage capacity due to phase change fusion and near-isothermal heat transfer characteristics of latent heat storage in the selected PCM-filled PBTES, temperature at the outlet of the PBTES during the system discharging is higher. It indicates that after the system discharging, the selected PCM-filled PBTES has better capability to maintain the high degree of temperature stratification which is built in the system charging. Higher temperature at the outlet of PBTES means more exergy input to turbine, and theoretically more electricity generable. It is shown in Fig. 13(d) that the discharging temperature of air at the outlet of the selected PCM-filled PBTES in the steady-state cycle is about 580 K which is the melting temperature of the selected PCM, and the discharging temperature is about 500 K in the rock-filled PBTES.

As a consequence, the inflow air with different temperature performs differently in the downstream turbine. Simulated efficiency profiles and power profiles of the turbine are plotted in Fig. 14, in which both systems with the rock-filled and the PCM-filled PBTES are included. The output power is regulated with respect to the inflow air temperature. At the beginning, due to thermal inertia of the PBTES, inflow temperature gradually increases to the rated value. Consequently, the power output starts at 60 kW at the first cycle, rumps up to 70 kW at the second cycle, and then stays at the rated 80 kW.

Although the two systems with different PBTES fillings have the same profile of power output, the performance of the turbine is different. In both systems, the turbine is operated in an operational window. Between operations with different power outputs, efficiency of the turbine is higher when the power is close to the rated value. Due to the varied inflow air temperature in every cycle, the efficiency of the turbine decreases with the decreasing air temperature. At the system level, the operational pattern of the turbine becomes stable when the system is at its steady-state, which are shown in Fig. 14 (b). Additionally, efficiency decreases differently due to different dynamics of heat storage. Taking advantage of the small reduction of the outlet air temperature of the PCM-filled PBTES during system discharging and the isothermal phase changing characteristics, the turbine efficiency of the system reduces to about 80% and maintained the efficiency for a while. In contrast, turbine

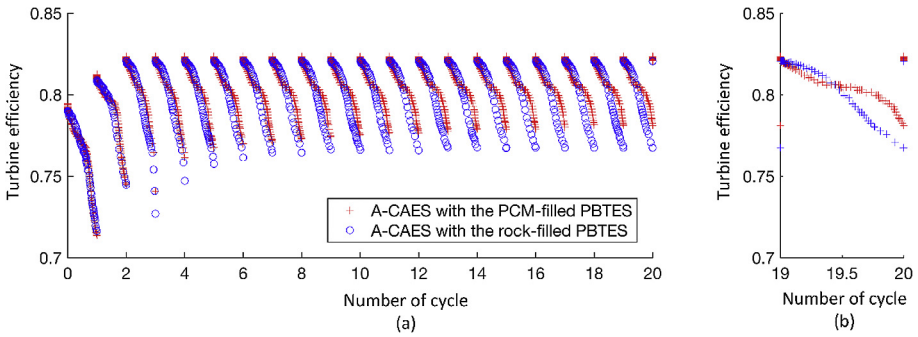


**Fig. 14.** Turbine efficiency profiles.

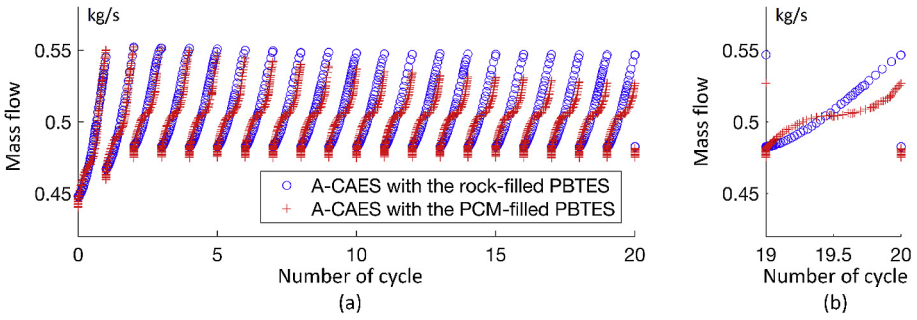


**Fig. 15.** Turbine mass flow rate profiles.

efficiency of the system with the rock-filled PBTES monotonously decreases to about 76%.

Furthermore, the simulated mass flow rates are plotted in Fig. 15. As output power of the turbine is regulated, the high efficiency of the turbine results in less mass flow required to generate the given rating power. As shown in Fig. 15(a), mass flow rate becomes smaller in a single cycle when the system approaches the steady-state operation in both systems. Because the turbine performs more effectively in the system with the PCM-filled PBTES during the steady-state cycles, it has a decreased steady-state mass flow rate profile compared to the system with the rock-filled PBTES, as shown in Fig. 15(b). With the same air volume/mass stored in the air tank, the reduction of the mass flow rate during the system discharging in these cycles leads to the increased duration of the system discharging and more work generated by the turbine.

Depending on the components' performance, therefore, overall cycle efficiency profiles of the two systems are plotted in Fig. 16. Cycle efficiency of the system with the selected PCM-filled PBTES has higher value than that of the system with the rock-filled PBTES. Steady-state cycle efficiencies of the systems with the latent heat storage and the sensible heat storage are about 56.5% and 53.2% respectively. Because of the same operations of the compressor during the charging period, increase of round-trip efficiency in the system with latent heat storage is mainly contributed by the improved turbine performance.

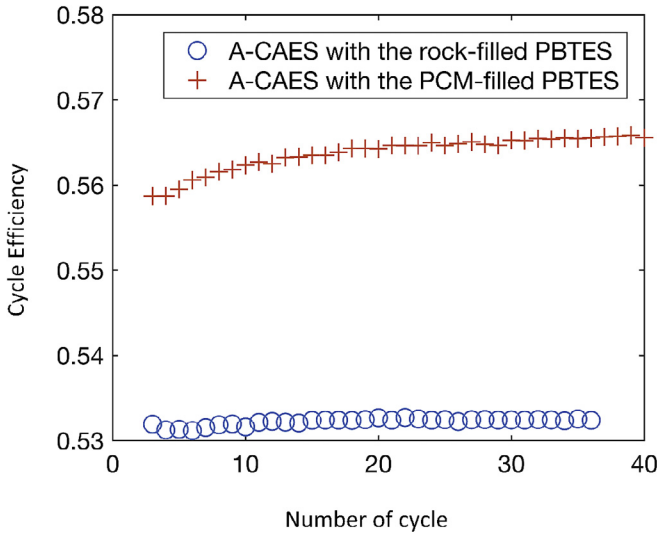


**Fig. 16.** System cycle efficiency.

## 6. Conclusion

This study presents a detailed system modelling framework which is a methodology to investigate the transient performance of the A-CAES system with PBTES. First, the mathematical models of reciprocating compressor, PBTES, isochoric air storage tank, and radial turbine are introduced. Then, using these models, simulations of the transient operations of both the components and the system are developed. According to the results, some conclusions can be drawn:

1) By comparing the simulation results with experimental data from the literature, models of the major components, including reciprocating compressor, PBTES, radial turbine and air storage tank, were validated. A time-variant system modelling framework was built on the resolved time-variant performance variations of the components;
2) The system modelling framework linked the performance between components, and bridged the dynamic performance variations between the system and the components;
3) In the studied system, the PCM filled heat storage was capable of saving around 43.5% of volume of the rocked-filled PBTES to achieve a similar energy storage capacity;
4) The PCMs improved the temperature stratification of the TES particles and reduced the energy losses of thermal storage. The maintained high degree of temperature stratification by the PCM-filled PBTES led to the high inlet air temperature of the radial turbine. The enhanced inflow air exergy improved both the turbine and whole system performance. Based on the simulation results, the efficiency of the radial turbine reduced slowly to the steady-state value and stayed at the values close to 80% for most of the operation due to the isothermal heat transfer of the PCM. In contrast, the turbine efficiency reduced monotonously to about 76% in the A-CAES system with the rock-filled PBTES. After all, the system cycle efficiency of the system with the PCM-filled heat storage is about 56.5% at the steady-state cycle. It is higher than the system with the rock-filled PBTES.

## Acknowledgement

Thanks to the funding support from Engineering and Physical Sciences Research Council (EPSRC), UK (EP/L014211/1, EP/L019469/1 and EP/K002228/1). The authors also want to thank the support from China 973 Research Programme (2015CB251301) to enable the discussion with Chinese partners.

## References

[1] Chen H, Cong TN, Yang W, Tan C, Li Y, Ding Y. Progress in electrical energy storage system: a critical review. Prog Nat Sci 2009;19:291–312.
[2] Curran H. Use of organic working fluids in Rankine engines. Columbia, MD

(USA): Hittman Associates, Inc.; 1979.
[3] Garvey SD, Pimm A. Chapter 5-compressed air energy storage A2-Letcher, Trevor M. Storing energy. Oxford: Elsevier; 2016. p. 87–111.
[4] Luo X, Wang J, Krupke C, Wang Y, Sheng Y, Li J, et al. Modelling study, efficiency analysis and optimisation of large-scale Adiabatic Compressed Air Energy Storage systems with low-temperature thermal storage. Appl Energy 2016;162:589–600.
[5] Wang S, Zhang X, Yang L, Zhou Y, Wang J. Experimental study of compressed air energy storage system with thermal energy storage. Energy 2016;103:182–91.
[6] Barbour E, Mignard D, Ding Y, Li Y. Adiabatic Compressed Air Energy Storage with packed bed thermal energy storage. Appl Energy 2015;155:804–15.
[7] Wolf D. Methods for design and application of adiabatic compressed air energy: storage based on dynamic modeling. Laufen. 2011.
[8] Peng H, Dong H, Ling X. Thermal investigation of PCM-based high temperature thermal energy storage in packed bed. Energy Convers Manag 2014;81:420–7.
[9] Peng H, Li R, Ling X, Dong H. Modeling on heat storage performance of compressed air in a packed bed system. Appl Energy 2015;160:1–9.
[10] Peng H, Yang Y, Li R, Ling X. Thermodynamic analysis of an improved adiabatic compressed air energy storage system. Appl Energy 2016;183:1361–73.
[11] Sciacovelli A, Li Y, Chen H, Wu Y, Wang J, Garvey S, et al. Dynamic simulation of Adiabatic Compressed Air Energy Storage (A-CAES) plant with integrated thermal storage – link between components performance and plant performance. Appl Energy 2017;185(Part 1):16–28.
[12] Khudhair AM, Farid MM. A review on energy conservation in building applications with thermal storage by latent heat using phase change materials. Energy Convers Manag 2004;45:263–75.
[13] Sarı A. Thermal reliability test of some fatty acids as PCMs used for solar thermal latent heat storage applications. Energy Convers Manag 2003;44:2277–87.
[14] Michels H, Pitz-Paal R. Cascaded latent heat storage for parabolic trough solar power plants. Sol Energy 2007;81:829–37.
[15] Stouffs P, Tazerout M, Wauters P. Thermodynamic analysis of reciprocating compressors. Int J Therm Sci 2001;40:52–66.
[16] Kang SH. Design and experimental study of ORC (organic Rankine cycle) and radial turbine using R245fa working fluid. Energy 2012;41:514–24.
[17] Yang J, Pu L, Wang Z, Zhou Y, Yan X. Fault detection in a diesel engine by analysing the instantaneous angular speed. Mech Syst signal Process 2001;15:549–64.
[18] Kornhauser A, Smith J. Application of a complex Nusselt number to heat transfer during compression and expansion. J heat Transf 1994;116:536–42.
[19] Adair R, Qvale E, Pearson JT. Instantaneous heat transfer to the cylinder wall in reciprocating compressors. 1972.
[20] Disconzi FP, Deschamps CJ, Pereira EL. Development of an in-cylinder heat transfer correlation for reciprocating compressors. 2012.
[21] Tuhovcak J, Hejcik J, Jicha M. Comparison of heat transfer models for reciprocating compressor. Appl Therm Eng 2016;103:607–15.
[22] Kornhauser AA, Smith JJL. The effects of heat transfer on gas spring performance. J Energy Resour Technol 1993;115:70–5.
[23] Mathie R, Markides CN. Heat transfer augmentation in unsteady conjugate thermal systems – Part I: semi-analytical 1-D framework. Int J Heat Mass Transf 2013;56:802–18.
[24] Hu J, Yang L, Shao L-L, Zhang C-L. Generic network modeling of reciprocating compressors. Int J Refrig 2014;45:107–19.
[25] Dixon S. Fluid mechanics, thermodynamics of turbomachinery. in si/metric units. 1978.
[26] van Putten H, Colonna P. Dynamic modeling of steam power cycles: Part II – simulation of a small simple Rankine cycle system. Appl Therm Eng 2007;27:2566–82.
[27] Dixon SL, Hall C. Fluid mechanics and thermodynamics of turbomachinery. Butterworth-Heinemann; 2013.
[28] Wallace F. Theoretical assessment of the performance characteristics of inward radial flow turbines. Proc Inst. Mech Eng 1958;172:931–52.
[29] Yang J, Wang J, Bu S, Zeng M, Wang Q, Nakayama A. Experimental analysis of forced convective heat transfer in novel structured packed beds of particles. Chem Eng Sci 2012;71:126–37.
[30] Anderson R, Shiri S, Bindra H, Morris JF. Experimental results and modeling of energy storage and recovery in a packed bed of alumina particles. Appl Energy 2014;119:521–9.
[31] Peng H, Yang Y, Li R, Ling X. Thermodynamic analysis of an improved adiabatic compressed air energy storage system. Appl Energy 2016;183:1361–73.
[32] Andersen KT. Theory for natural ventilation by thermal buoyancy in one zone with uniform temperature. Build Environ 2003;38:1281–9.
[33] Zanganeh G, Pedretti A, Zavattoni S, Barbato M, Steinfeld A. Packed-bed thermal storage for concentrated solar power – pilot-scale demonstration and industrial-scale design. Sol Energy 2012;86:3084–98.
[34] Raju M, Kumar Khaitan S. Modeling and simulation of compressed air storage in caverns: a case study of the Huntorf plant. Appl Energy 2012;89:474–81.
[35] Bell IH, Wronski J, Quoilin S, Lemort V. Pure and pseudo-pure fluid thermophysical property evaluation and the open-source thermophysical property library CoolProp. Ind. Eng Chem Res 2014;53:2498–508.
[36] Mertens N, Alobaid F, Frigge L, Epple B. Dynamic simulation of integrated rock-bed thermocline storage for concentrated solar power. Sol Energy 2014;110:830–42.
[37] Izquierdo-Barrientos MA, Sobrino C, Almendros-Ibáñez JA. Thermal energy storage in a fluidized bed of PCM. Chem Eng J 2013;230:573–83.
[38] Crotogino F, Mohmeyer K-U, Scharf R, Huntorf CAES. More than 20 years of successful operation. Orlando, Florida, USA. 2001.
[39] Jones AC. Design and test of a small, high pressure ratio radial turbine. ASME 1994 International Gas Turbine and Aeroengine Congress and Exposition: American Society of Mechanical Engineers. 1994. p. V001T01A45–VT01A45.
[40] Meier A, Winkler C, Wuillemin D. Experiment for modelling high temperature rock bed storage. Sol Energy Mater 1991;24:255–64.
[41] McTigue JD, White AJ, Markides CN. Parametric studies and optimisation of pumped thermal electricity storage. Appl Energy 2015;137:800–11.
[42] Xu C, Wang Z, He Y, Li X, Bai F. Sensitivity analysis of the numerical study on the thermal performance of a packed-bed molten salt thermocline thermal storage system. Appl Energy 2012;92:65–75.
[43] Agyenim F, Hewitt N, Eames P, Smyth M. A review of materials, heat transfer and phase change problem formulation for latent heat thermal energy storage systems (LHTESS). Renew Sustain energy Rev 2010;14:615–28.
[44] White AJ, McTigue JD, Markides CN. Analysis and optimisation of packed-bed thermal reservoirs for electricity storage applications. 2016.